RESEARCH ON A NUMERICAL MODEL OF REAL MESO-STRUCTURES IN THE NON-SHEAR ZONE OF CLAY

RAZISKAVA NUMERIČNEGA MODELA REALNIH MEZO-STRUKTUR V NE-STRIŽNEM DELU GLINE

Wei Wang *(corresponding author)*
Nanjing Institute of Technology,
Institute of Civil Engineering and Architecture
211167, Nanjing, China
E-mail: ww1177114@163.com

Binghua Zhao
Nanjing Institute of Technology,
Institute of Civil Engineering and Architecture
211167, Nanjing, China

Liwu Yu
Nanjing Institute of Technology,
Institute of Civil Engineering and Architecture
211167, Nanjing, China

Deheng Zhang
Nanjing Institute of Technology,
Institute of Civil Engineering and Architecture
211167, Nanjing, China

DOI https://doi.org/10.18690/actageotechslov.16.2.66-76.2019

Keywords

clay; mesoscopic model; numerical analysis; real meso-structures

Ključne besede

glina; mezoskopski model; numerična analiza; realne mezostrukture

Abstract

The conventional numerical simulations of rock and soil are mainly concerned with the macroscopic continuous model or the pseudo-microscopic model established using the discrete-element method (DEM). However, these adopted models are not completely consistent with actual soil samples. To explore the evolution law of the internal stresses of soil samples from the mesoscopic perspective, we proposed an image-finite-element method for studying the deflection angles and the shear stresses at four points in the non-shear zone of clay with real mesostructures. The approach allowed for a realistic distribution of the pore structures and avoided any virtualization, thereby significantly improving the veracity of the mesoscopic model. It worked by using a microscopic lens and a charge-coupled device (CCD) to capture the two-dimensional (2D) meso image in the non-shear zone, and then convert this digital image into a vector image recognized by the finite-element software (ABAQUS) through image-processing techniques, and import it into a numerical model, and then carry out a numerical calculation. For the purposes of performing a

Izvleček

Konvencionalna numerična simulacija kamnin in zemljin se v glavnem ukvarja z makroskopskim kontinuiranim modelom ali psevdo-mikroskopskim modelom, določenim z metodo diskretnih elementov (DEM). Ti modeli niso popolnoma skladni z dejanskimi vzorci zemljin. Za raziskavo pravila napredovanja notranjih napetosti vzorcev zemljin iz mezoskopske perspektive, predlagamo slikovno metodo končnih elementov za proučevanje odklonskih kotov in strižnih napetosti na štirih mestih v ne-strižnem delu gline z realnimi mezostrukturami. Takšen pristop omogoča realistično porazdelitev struktur por in preprečuje virtualizacijo, kar bistveno izboljša verodostojnost mezoskopskega modela. Deluje z uporabo mikroskopskih leč in senzorjem CCD za zajemanje dvodimenzionalne (2D) mezo-slike v ne-strižnem območju in nato pretvorbo te digitalne slike v vektorsko sliko. S tehnikami obdelave slik jo prepozna programska oprema s končnimi elementi (ABAQUS), uvozimo jo v numerični model, nato pa izvedemo numerični izračun. Za izvedbo korelacijske analize je bil na istem vzorcu

correlation analysis, the unconfined-compression (UC) test was also carried out on the same specimen. The numerical results show that there is no shear failure in the meso numerical model, which is consistent with the UC test results for the same region. And, the quantitative analysis results show that: (1) under load, the yield zones in the meso numerical model are obviously located around the pores; (2) the evolution laws of the deflection angles and the meso shear stresses at four points are different in the compression process; and (3) the pore structures play a significant role in the evolution of the deflection angles and meso shear stresses, especially around the larger and denser pores.

opravljen tudi enoosni preizkus (UC). Numerični rezultati kažejo, da v mezo-numeričnem modelu ni strižne porušitve, kar je skladno z rezultati enoosnega preizkusa v istem območju. Rezultati kvantitativne analize kažejo: (1) da so pod obremenitvijo plastična območja v mezo--numeričnem modelu očitno locirana okoli por; (2) da se pravila napredovanja odklonskih kotov in mezo-strižnih napetosti v štirih točkah v procesu stiskanja razlikujejo; in (3) da imajo strukture por pomembno vlogo pri povečanju odklonskih kotov in mezo-strižnih napetosti, zlasti okoli večjih por in gosteje razporejenih por.

1 INTRODUCTION

Understanding the connection between internal stresses from the mesoscopic perspective and the shear failure mechanism of soil is a fundamental challenge in geomechanics research. Works on the theory, testing and numerical simulations of soil from microscopic and macroscopic perspectives have led to many great achievements. For example, in theory, Borja et al. investigated the effect of the spatially varying degree of saturation on triggering a shear band in granular materials and presented variational formulations for the porous solids whose voids were filled with liquid and gas [1]. Lu and Yang pointed out that the development of shear bands was affected by the coupling strain rate and pore pressure of a material using the momentum equations of water and grains by the mixture theory [2]. Gutierrez introduced a simple elastoplastic constitutive model that adequately captured the monotonic response of granular soils under biaxial loading conditions and developed a strain-localization criterion expressed in terms of constitutive parameters [3]. As a matter of fact, these theoretical studies take into account the effects of the physical properties of the particles and macroscopic parameters on the shear failure of soil samples [4], but do not involve the influence of internal stresses from the mesoscopic perspective. In tests, developments in meso experimental techniques, like scanning electron microscopy (SEM), computer tomography (CT), ultrasonic or digital camera, etc., made the real microscopic features of soil samples more deeply understood. Most importantly, these techniques enable the precise detection of the particles' (or aggregate particles') morphology, providing a detailed position of the local pores. The observations, made by Shan et al, indicate that the soil particles were rearranged in an orientation parallel to the direction of the maximum principal stress and the maximum shear stress [5]. Bo et al. demonstrated how to determine the mineralogical properties of ultra-soft soils using X-ray diffraction and scanning electron microscope techniques [6]. Zhang et al. calculated the volume porosity of the whole specimen by analyzing the tomography images with an error of only 3.93% compared with the experimental porosity [7]. However, compared with the digital camera method, the complexity of the soil samples' preparation and the high cost of the test equipment mentioned above limit their application. For this reason, a digital camera or a microscope lens were another choice for revealing the mesostructures of geomaterials [8-10]. Yue Z Q et al. carried out quantitative investigations of the orientations, distributions and shapes of aggregates about asphalt concrete using a conventional digital camera [11]. Ghalehjough et al. showed that the shear failure mechanism of the soil changed from general towards punching shear failure with increasing particle roundness by analysing the photographs taken from a high-resolution digital camera [12]. Shao et al. developed a series of geotechnical test instruments based on a digital image measurement system [13]. Amy et al. found that the shear band thickness ranged between 6 and 9.5 times D50 and pointed out that the grain shape, angularity, and size distribution can also affect the shear band thickness using the digital image correlation (DIC) method [14]. Although the aforementioned image methods have successfully obtained the mesostructures of soil and investigated its influence on the macroscopic properties, these results only focus on the particle characteristics of the soil and do not take into account the influence of the internal pore characteristics, nor do they involve the internal stresses from the mesoscopic perspective. In numerical simulations, some researchers have simulated the effect of mesoscopic characteristics on the macro performance by setting a "weak" element in the finite-element software. For instance, Jiang et al. performed a series of biaxial-compression-test simulations by increasing the void ratio of element No.105 on methane hydrate-bearing sediment samples to simulate

the influence of the nonuniform density (mesostructures) and showed that the bifurcation of the stress and volumetric response of the elements within the shear band is more obvious during the tests [15]. Certainly, the most typical method for simulating the microscopic model of soil is DEM, which helps to study the deformation behaviour of the particle system. Bayesteh et al. developed a 2D DEM computer program to simulate the mechanism that controlled the behaviour of a granular assembly after local and random particle loss [16]. Nicot et al. discussed the dependency of the mechanical response to the imposed volumetric strain by presenting the numerical simulation with a discrete element model and micromechanical approaches [17]. Li et al. showed that it was possible to capture, using DEM, the essential features of the mechanical behaviour of granular materials under a complex stress state [18]. However, the DEM method mainly simulates granular materials, such as sand, soil-rock mixtures, and concrete, and assumes that the soil particles are rigid spheres adopted in the numerical model, which is not in accordance with the mechanical properties of actual geomaterials.

In short, the mesoscopic mechanism of the soil samples' macroscopic properties, especially the evolution laws of the internal real meso structure and its meso stress, need to be further studied. To address the issue, this paper introduced an image-finite-element method (IFEM) on the basis of previous achievements [19]. It incorporated a real meso image and a finite-element model, respectively, for investigating the evolution of the deflection angles and the internal stresses from a mesoscopic perspective on the unconfined compression simulation test. Due to the large magnification of the microscopic imaging system, the acquisition field of view is small and it is difficult to locate exactly the position of the initiation of the shear band. Therefore, the evolution of the internal stresses from the mesoscopic perspective in the non-shear zone was studied in this paper. As for the evolution of the internal stresses in the shear zone, it needs to be studied after the equipment is improved in the next step.

2 UNCONFINED-COMPRESSION SIMULATION TEST

Because the unconfined-compression (UC) test is by far the most popular technique for soil shear testing, this paper uses the UC test and the mesoscopic image-acquisition system to form a set of soil samples for the macro and micro test equipment (see Figure 1), which cannot only obtain the clay meso image conveniently, but also carry out the macroscopic compression test at the same time. In this way, the numerical results and the experimental results can be compared and analyzed.

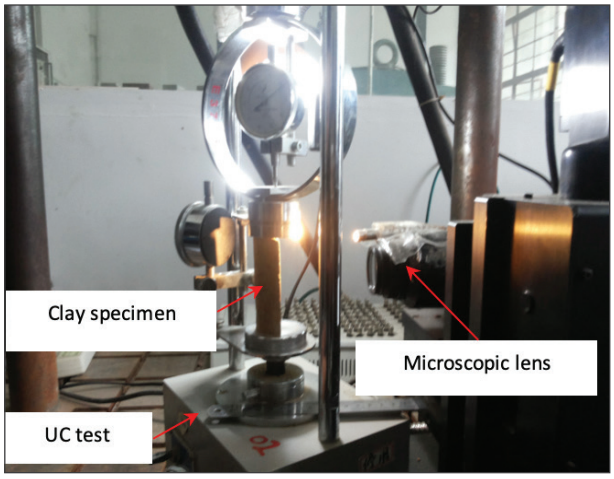

Figure 1. Equipment combining microscopic lens and UC test.

2.1 Clay sample preparation

The materials used in the test were clay, which was quarried from a construction site around the Nanjing Institute of Technology. Its plastic limit and liquid limit values were 18.36 and 39.14, respectively. The traditional cylindrical clay sample was divided into two parts from the symmetrical surface and the semi-cylindrical shape was taken as the test object (see Figure 2). The semi-cylindrical clay sample was placed on the pedestal of the UC test, and the symmetrical plane was thrown directly at the microscopic lens.

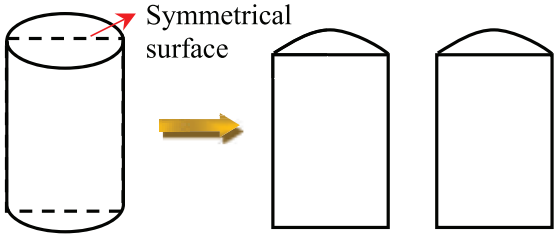

Figure 2. Schematic diagram of a clay sample divided into two parts.

2.2 Mesoscopic image acquisition

Since the surface of the cylindrical clay sample is curved, it is not convenient to collect images using the mesoscopic acquisition system with a microscopic lens and a CCD. According to the axisymmetric principle, the symmetrical surface of a semi-cylindrical clay sample was selected as the observation surface. This not only ensures that the observed area is plane, but also can collect the mesoscopic characteristics of the clay. So, the tests were carried out on the air-dried clay samples (not considering

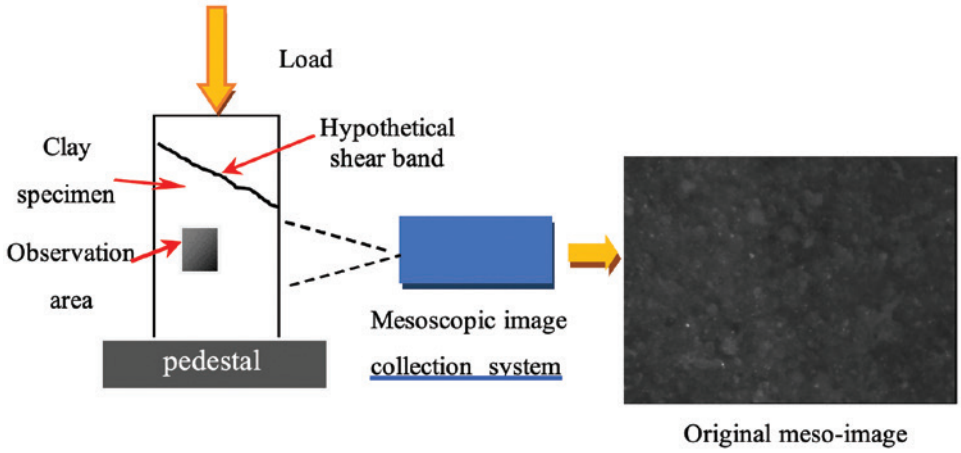

Figure 3. The original meso-image acquistion diagram.

the influence of pore water) with a 39.1-mm diameter and an 80-mm height. Then, the original images (768×576 pixels) with real mesoscopic features before loading were obtained using the mesoscopic acquisition system. Figure 3 shows a schematic diagram of the image collected by the mesoscopic acquisition system (the image has a physical resolution of 0.0014 mm).

2.3 Image processing

The original meso image contains the true distribution characteristics of the clay particle aggregates and pores, which is the basis for establishing the meso numerical model. In order to embody the mesoscopic information in the numerical model, it is also necessary to pre-process the meso image, including denoising and binarization. The image data can be affected by the noises from the device elements and the surrounding lights. Since the adaptive median filter algorithm can preserve the edges in an image, it was chosen for the de-noise operation in this paper. For studying the effects of internal stresses and pores, it is necessary to distinguish the particle aggregates from the pores, so the particle aggregates and pores were expressed in black and white using Otsu's binarization method, respectively. In fact, Otsu's method is an image binarization technique, which cannot only avoid the interference of artificial factors, but also automatically calculates the maximum threshold of intra-class variances. In this way, the real boundaries of the clay particle aggregates and pores were fully identified. The threshold of the meso image was obtained using the formula (1).

$$Q(k)=\frac{(Ave\times W(k)-Aver(k))^2}{W(k)\times(1-W(k))} \qquad (1)$$

where $Q(k)$ is the separation index of the grey class; *Ave* is the average of the grey-value; *Aver* and $W(k)$ are, respectively, the mean of the grey-level class and the sum of the grey-class histograms, which can be calculated via the equations

$$Aver(k)=\sum_{i=0}^{k}(i+1)Phs(i) \quad \text{and} \quad W(k)=\sum_{i=1}^{k}Phs(i)\ ;$$

$Phs(i)$ is the probability function of the grey level; i is the grey level, and $0 \le i \le 255$. When the $Q(k)$ value is the largest, the optimal threshold (T) is found. That is $T=k-1$. Obviously, the threshold values of the meso images are entirely different. In this study, the meso image threshold was 0.1775. So, the meso image can be processed using Otsu's method after the median filtering and the binary resultant image was obtained successfully (see Figure 4).

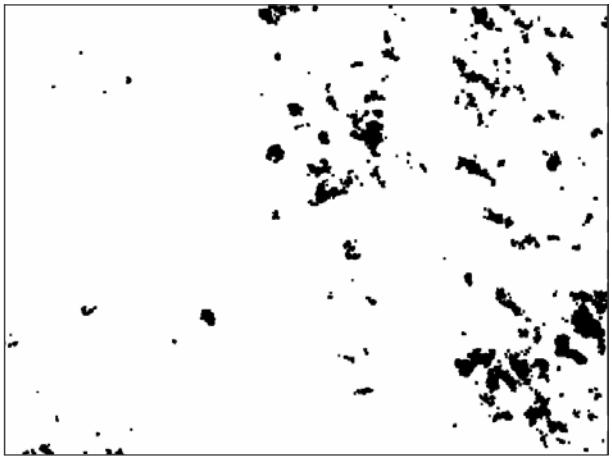

Figure 4. Binary resultant image.

2.4 Establishing the numerical model

Because the meso image is a digital image and cannot be identified by the finite-element software, it is necessary to vectorize the digital image. With the help of vector

software CorelDRAW, the digital image can be converted into a vector graph, and the numerical model containing the pore meso features can be established by importing the finite-element software (ABAQUS). In this way, the 2D numerical model with the clay real mesostructures was established successfully. Figure 5(a) shows the numerical model and Figure 5(b) gives the mesh result using the triangular element.

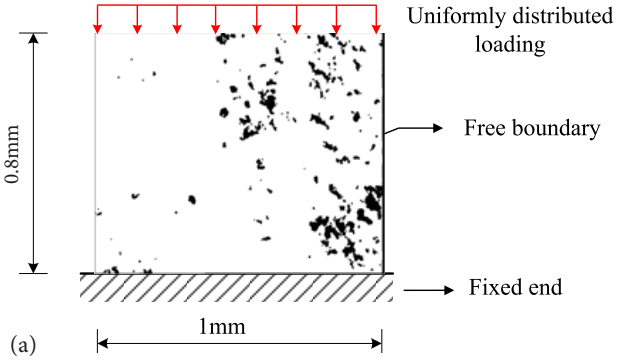

Figure 5. (a) Numerical model; (b) mesh resultant.

3 NUMERICAL ANALYSES AND RESULTS

3.1 Determination of the model parameters and the boundary conditions

In this paper, the internal stresses evolution of the air-dried clay under uniaxial compression considering the effect of pore meso characteristics is discussed. Therefore, it was assumed that the clay sample was in accordance with the Mohr-Coulomb model. The model is easy for obtaining the parameters of the material required by the finite-element software (ABAQUS) using the triaxial drained test: cohesion (c) and friction angle (φ, no dilatancy here), which is, respectively, adopted as 50 KPa and 28.51°. According to the UC test conditions, the boundary conditions of the numerical model were set up, as shown in Figure 5(a). Then, the compression process of the clay sample can be simulated by applying the same load as the UC test.

3.2 Simulation results

Based on the numerical results of the Mohr-Coulomb model, the partial regions (the red parts shown in Figure 6) present the shear yield. This is due to the fact that the shear stress in this part of the region exceeds the shear yield stress, while the others are still in an elastic state, such as the blue region shown in Figure 6. It can be seen that there is only a local yield and no through shear band in the observed region collected by the mesoscopic acquisition system, which qualitatively indicates that the numerical simulation results of the region are consistent with those of the UC test in the same region. In addition, it can be seen from Figure 6 that the yield regions are mostly like an "X" shape and mainly distributed near larger pores.

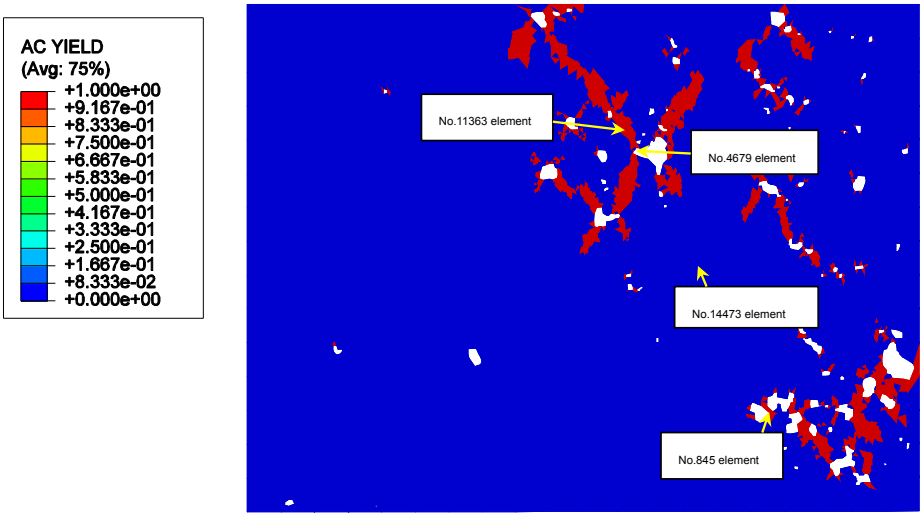

Figure 6. Profile of shear yield area.

In order to study the evolution of the internal stresses from the mesoscopic perspective, four typical points were selected, as shown in Figure 6. The first point is marked No. 4679 element in the blue region of a large pore boundary. The second point is labelled No. 845 element in a band of the red region between the two pores. The third point is located in the blue area away from the pores and labelled as the No.14473 element. The last one labelled No.11363 element is in the red region near a pore. Here are the quantitative results of the four points of the minor principle stress (σ_3), the major principle stress (σ_1), the shear stress (τ), the normal stress (σ), the shear strength (τ_f), and the deflection angle (θ).

By using the image-finite-element method, the minor principle stress, the major principle stress and the shear stress of the whole field in the observed area can be directly obtained. Tables 1 and 2 show the results at only four points. It can be seen from the data in the table that the stress values at each point are not only different but also positive and negative. It is shown that the stress states of each point are different from the mesoscopic perspective, which should be the result of the influence of the pore structures. Although it is also in the blue region, the major principle stress at point No. 4679 near the pore is about 2–2.5 times the value of the major principle stress at the No. 14473 point, far away from the pore. Similarly, even in the red region, the point No.

Table 1. Quantitative results of two points located in the red region.

Time (*s*)	NO. 845 element						NO. 11363 element					
	σ_3 (KPa)	σ_1 (KPa)	τ (KPa)	σ (KPa)	τ_f (KPa)	θ	σ_3 (KPa)	σ_1 (KPa)	τ (KPa)	σ (KPa)	τ_f (KPa)	θ
0.010	-0.47	-15.75	4.84	14.02	57.44	19.67	1.12	-6.11	1.34	5.72	53.04	16.31
0.020	-0.94	-31.41	9.69	27.92	64.82	19.77	2.26	-12.23	2.69	11.44	56.07	16.36
0.035	-1.60	-54.72	17.00	48.57	75.78	19.91	3.98	-21.42	4.73	20.03	60.63	16.44
0.058	-2.51	-89.27	28.01	79.02	91.94	20.12	6.61	-35.25	7.82	32.93	67.48	16.57
0.091	-4.13	-140.19	43.87	124.16	115.91	20.09	10.70	-56.13	12.56	52.34	77.78	16.80
0.104	-4.82	-159.22	49.74	141.06	124.88	20.07	12.35	-64.04	14.40	59.65	81.66	16.94
0.105	-4.81	-160.98	50.31	142.61	125.70	20.07	12.52	-64.79	14.57	60.35	82.03	16.95
0.105	-4.81	-161.02	50.32	142.64	125.72	20.07	12.52	-64.81	14.58	60.36	82.04	16.95
0.105	-4.81	-161.08	50.34	142.69	125.75	20.07	12.53	-64.83	14.58	60.39	82.06	16.95
0.105	-4.80	-161.17	50.37	142.77	125.79	20.07	12.54	-64.87	14.59	60.43	82.08	16.96
0.105	-0.57	-169.69	55.89	148.58	128.87	20.70	12.58	-64.94	14.62	60.48	82.10	16.99
0.105	-0.58	-169.73	55.91	148.60	128.88	20.70	12.60	-65.03	14.64	60.56	82.15	16.99
0.106	-0.60	-169.79	55.95	148.64	128.90	20.71	12.63	-65.16	14.67	60.68	82.21	16.99
0.106	-0.63	-169.88	56.00	148.69	128.93	20.73	12.67	-65.36	14.72	60.87	82.31	16.99
0.106	-0.68	-170.01	56.09	148.77	128.97	20.75	12.74	-65.66	14.79	61.14	82.46	17.00
0.107	-0.76	-170.22	56.21	148.89	129.04	20.79	12.84	-66.11	14.89	61.56	82.68	17.00
0.108	-0.86	-170.52	56.38	149.07	129.13	20.84	12.99	-66.79	15.04	62.19	83.01	17.01
0.110	-1.01	-170.95	56.63	149.32	129.26	20.91	13.21	-67.81	15.28	63.13	83.51	17.02
0.112	-1.23	-171.57	57.00	149.69	129.46	21.01	13.56	-69.34	15.63	64.55	84.26	17.05
0.116	-1.55	-172.48	57.52	150.22	129.74	21.16	14.07	-71.63	16.16	66.67	85.39	17.09
0.121	-0.86	-170.52	58.56	147.06	128.06	21.84	14.87	-75.09	16.97	69.85	87.08	17.16
0.129	-0.31	-168.96	58.83	145.05	126.99	22.13	16.08	-80.29	18.21	74.63	89.61	c
0.142	-0.20	-168.65	59.52	144.01	126.44	22.50	17.97	-88.15	20.09	81.83	93.44	17.47
0.160	-0.51	-169.53	60.57	143.95	126.41	22.90	21.12	-100.40	23.03	93.03	99.38	17.77
0.164	-0.66	-169.94	60.79	144.20	126.54	22.96	22.54	-104.11	24.05	96.26	101.10	18.08
0.169	-0.78	-170.28	60.98	144.38	126.64	23.02	22.16	-105.47	24.46	97.53	101.77	17.99
0.176	-0.65	-169.92	60.11	144.86	126.90	22.64	23.57	-101.51	27.15	90.50	98.04	22.09

Table 2. Quantitative results of two points located in the blue region.

Time (*s*)	NO. 4679 element						NO. 14473 element					
	σ_3 (KPa)	σ_1 (KPa)	τ (KPa)	σ (KPa)	τ_f (KPa)	θ	σ_3 (KPa)	σ_1 (KPa)	τ (KPa)	σ (KPa)	τ_f (KPa)	θ
0.010	-16.82	-13.59	3.94	12.10	56.42	20.72	-0.03	-5.46	0.18	5.45	52.89	1.87
0.020	-33.89	-27.20	7.94	24.17	62.83	20.92	-0.07	-10.91	0.36	10.90	55.79	1.91
0.035	-60.05	-47.67	14.05	42.22	72.41	21.21	-0.12	-19.10	0.65	19.08	60.13	1.97
0.058	-100.57	-78.48	23.46	69.17	86.72	21.66	-0.19	-31.39	1.12	31.35	66.64	2.06
0.091	-157.27	-121.25	37.54	105.55	106.03	22.69	-0.30	-49.90	1.90	49.82	76.45	2.20
0.104	-171.82	-133.87	42.52	115.48	111.30	23.40	-0.32	-56.88	2.22	56.80	80.15	2.25
0.105	-173.01	-135.16	43.11	116.40	111.79	23.52	-0.33	-57.55	2.25	57.46	80.50	2.25
0.105	-173.04	-135.19	43.13	116.43	111.80	23.53	-0.33	-57.56	2.25	57.47	80.51	2.25
0.105	-173.08	-135.24	43.15	116.46	111.82	23.53	-0.33	-57.58	2.25	57.50	80.52	2.25
0.105	-173.14	-135.31	43.18	116.51	111.84	23.54	-0.33	-57.62	2.25	57.53	80.54	2.25
0.105	-172.02	-135.73	43.58	116.62	111.91	23.68	-0.31	-57.67	2.28	57.58	80.56	2.28
0.105	-172.15	-135.87	43.65	116.73	111.96	23.70	-0.31	-57.75	2.28	57.65	80.60	2.28
0.106	-172.33	-136.10	43.76	116.88	112.04	23.72	-0.31	-57.86	2.29	57.77	80.67	2.28
0.106	-172.61	-136.44	43.92	117.12	112.17	23.76	-0.31	-58.04	2.29	57.95	80.76	2.28
0.106	-173.03	-136.94	44.17	117.47	112.35	23.81	-0.31	-58.30	2.31	58.21	80.90	2.28
0.107	-173.64	-137.70	44.54	117.99	112.63	23.88	-0.31	-58.69	2.33	58.60	81.11	2.29
0.108	-174.56	-138.84	45.09	118.78	113.05	24.00	-0.31	-59.29	2.35	59.19	81.42	2.29
0.110	-175.91	-140.54	45.91	119.94	113.67	24.17	-0.31	-60.18	2.40	60.09	81.90	2.30
0.112	-177.86	-143.06	47.15	121.66	114.58	24.43	-0.32	-61.53	2.46	61.43	82.61	2.30
0.116	-181.47	-146.74	48.75	124.38	116.02	24.66	-0.32	-63.55	2.55	63.45	83.68	2.31
0.121	-188.86	-151.37	50.43	128.08	117.99	24.80	-0.32	-66.60	2.69	66.49	85.29	2.33
0.129	-197.46	-158.94	53.50	133.86	121.06	25.13	-0.33	-71.17	2.91	71.05	87.72	2.36
0.142	-209.74	-169.86	58.06	142.01	125.38	25.64	-0.31	-78.11	3.27	77.97	91.39	2.41
0.160	-227.86	-185.52	64.78	153.39	131.42	26.40	-0.25	-88.83	3.84	88.66	97.06	2.49
0.164	-232.24	-190.16	67.05	156.40	133.02	26.74	-0.20	-91.58	4.00	91.40	98.52	2.51
0.169	-237.63	-194.77	69.31	159.33	134.58	27.09	-0.11	-94.39	4.19	94.20	100.00	2.55
0.176	-245.24	-200.93	72.57	162.86	136.45	27.69	0.22	-98.73	4.56	98.52	102.30	2.65

845 is significantly larger than the major principle stress at point No. 11363 because it is in a structure similar to a"slender column".

Then, using the following equation (2), which is transformed from the formula $\tau = \frac{\sigma_1 - \sigma_3}{2} sin\, 2\, \theta$, the deflection angle θ at four points can be solved at every loading state.

$$\theta = \frac{1}{2} arcsin \frac{2\tau}{\sigma_1 - \sigma_3} \qquad (2)$$

Figure 7 (a), (b), (c) and (d) are the evolution curves of the deflection angles inclined in the direction of the major principal plane, respectively. As shown in Figure 7, we can learn that, in both the red and blue regions, the deflection angles of the four points increase with the increasing load. Obviously, when the load is increased from 0 to 50% loads, although the initial deflection angle of each point is different, the evolution curve is an increasing trend, but the slope is different. This suggests that the equilibrium of the internal and external forces of the clay sample at this stage is realized by the clay particles' deflection. This is an interesting phenomenon. The deflection angle at point No. 845 is almost unchanged between 25% and 50% of the load, which may be a sign that the "slender column" reached a critical equilibrium. But, as the load continues to increase, the deflection angle at point No. 845 suddenly jumps significantly, and then increases rapidly until the maximum load. A small jump occurs at the point No. 4679 near the pore at 50% loads, like the point No. 845,

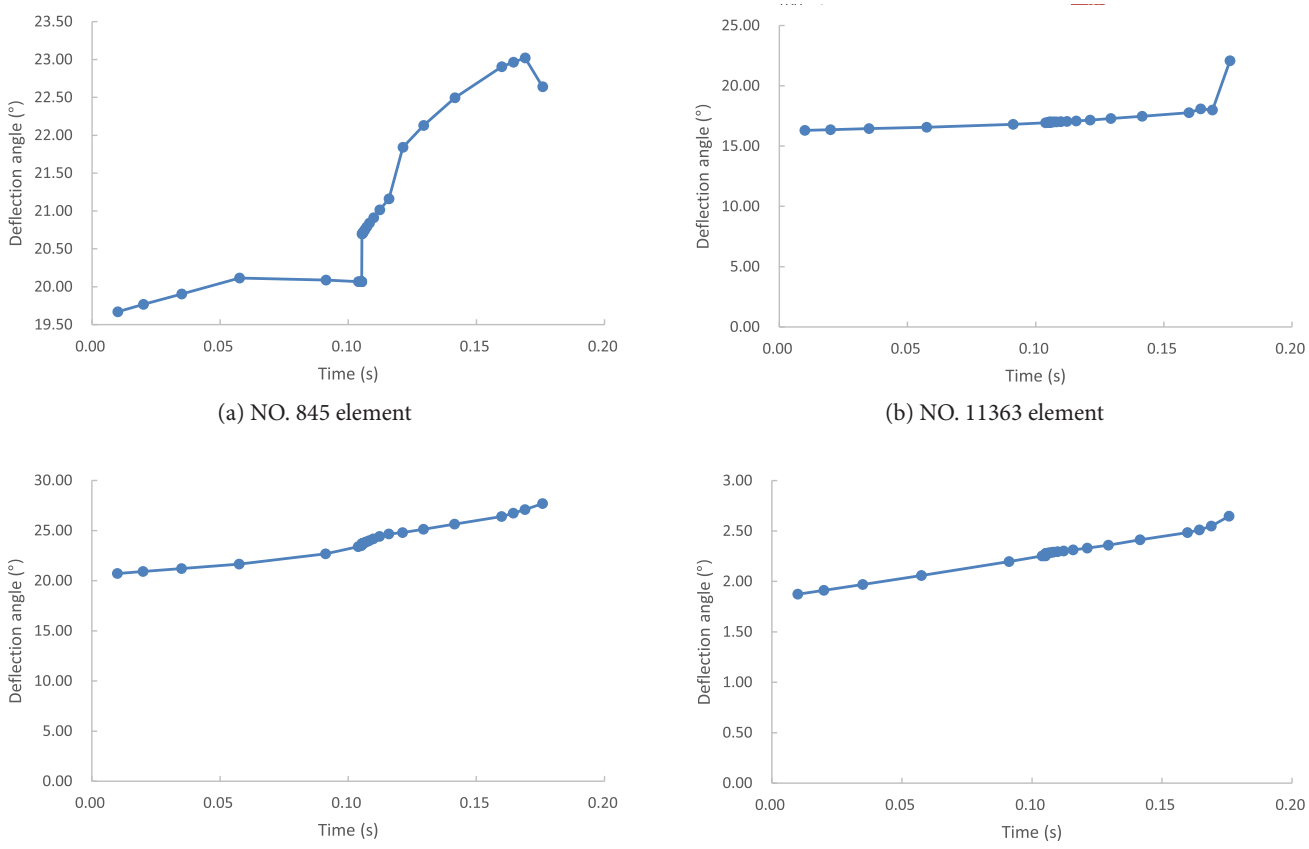

Figure 7. Evolution curves of deflection angle.

but not at the other two points. It can be seen that the mesoscopic pore characteristics will affect the movement of the clay particles. The curve slope of the point No. 845 after 50% loads is obviously higher than that of the other points, and the deflection angle is shifted from 20 degrees to 23 degrees. This indicates that there is a lack of effective constraints on the "slender column" in the area, which makes the clay particles deflect easily, thus exacerbating the growth of the major principal stress and the meso shear stress and making the region enter the plastic zone very quickly. Moreover, until near the maximum load, the deflection angle at the point No.11363 suddenly increased by 4 degrees, indicating that there might be a large dislocation at this point to cause small cracks. This might be due to the continued expansion of the local band plastic zone in which the point No. 11363 is located, as can be seen from Figure 6. In addition, the change in trend of the deflection angles at the two points No.4679 and No. 14473 in the blue region is relatively gentle, and the amplitude is not large. It can be seen that the blue part of the observed region is the main force-bearing body, which is called the main carrier, while the red part is the secondary carrier. From the above analysis, it can be concluded that the secondary carrier first enters the plastic zone under the action of the load, and gradually affects the main carrier through the adjustment until a new secondary carrier is formed. The main reason is that there are a number of weak structures in the clay sample, which are formed by the existence of pores.

Further, the normal stresses at the four points, given in Tables 1 and 2, were calculated using the following equation (3).

$$\sigma_n = \frac{\sigma_1+\sigma_3}{2} + \frac{\sigma_1-\sigma_3}{2} cos\, 2\,\theta \qquad (3)$$

Next, according to the Mohr-Coulomb yield theory, the shear strength at the four points can be drawn easily using the formula $\tau_f = c+\sigma_n \tan\varphi$. Figure 8 (a), (b), (c) and (d) show the curves of the meso shear stresses and the meso shear strengths at the four points with the increasing of loads, respectively. Figure 8 also describes the relationship between the meso shear stress and the meso shear strength at the same point. It can be seen from Figure 8 that the meso shear strength is obviously greater than that of the meso shear stress, indicating that the clay particle aggregates in the observed area are still able to withstand external loads. From Figure 8 (a) it can

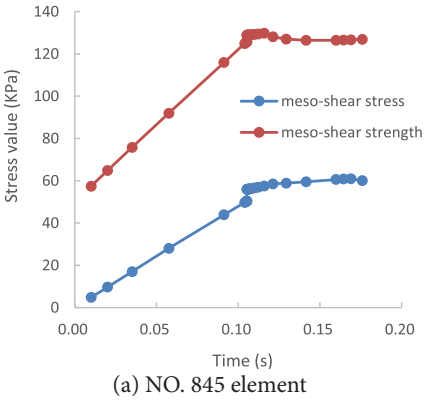

(a) NO. 845 element

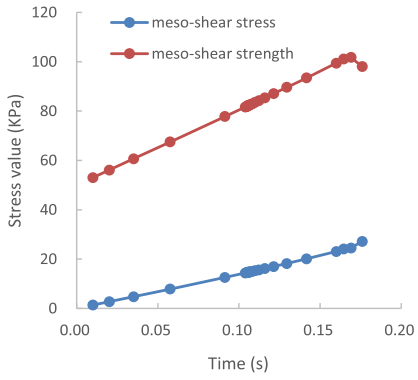

(b) NO. 11363 element

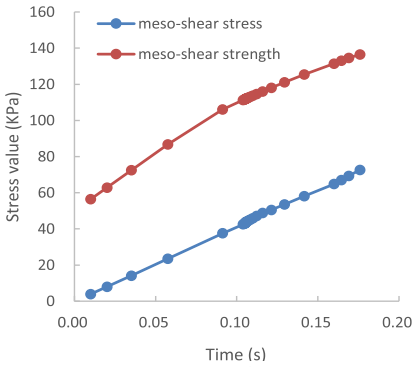

(c) NO. 4679 element

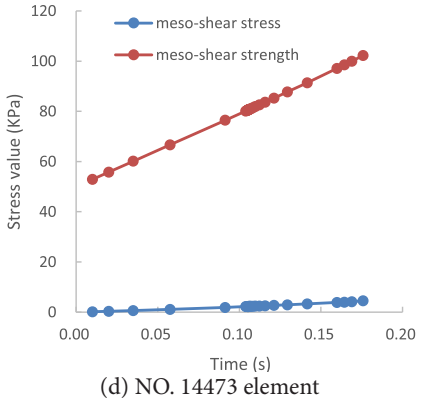

(d) NO. 14473 element

Figure 8. Profiles of meso shear stress and meso shear stress with load.

be seen that the variation curve of the meso shear stress and the meso shear strength at the point No.845 after 50% loads tends to be horizontal, which indicates that the stress state of the point No. 845 is no longer changing. Because there are pores on both sides of the site, the secondary carrier cannot affect the main carrier, and can only be connected with the main carrier through both ends. Therefore, after a certain degree of stress, the middle part cannot continue to bear a larger load. Figure 8 (b) shows that the meso shear strength at the point No.11363 begins to decrease near the maximum load, while the meso shear stress still keeps increasing. It can be seen that the dislocation of the clay particles can lead to the initiation of tiny cracks, but it does not cause damage. This is consistent with the previous conclusion. The curve slope of meso shear stress and meso shear strength at the point No.4679 is almost the same, shown in Figure 8 (c), and the final meso shear stress value is similar to that of the point No.845, which is related to the compactness degree of the clay particles weakened by its unilateral pores. A significant difference from the other points is that the meso shear stress at the point No.14473 is very slow to reach about 5 KPa (see Figure 8 (d)), which is slightly smaller than the shear strength 12 KPa of the clay sample obtained by the UC test. This indicates that the clay particle aggregates far away from pores are the main carrier, and the meso shear stress and the shear strength of the clay samples are basically in the order of magnitude. But the internal cause of shear failure of the clay samples is the evolution of secondary carriers. In short, some of the secondary carriers undergo adjustment, yielding to cracking until multiple subcarriers are connected to a single through shear band and destroyed. In fact, the meso numerical model is capable of withstanding loads, and mainly depends on the stress network intertwined by main carriers and secondary carriers. The evolution of the stress and strength in shear band should be further studied by improving the testing equipment and material parameters.

4 CONCLUSIONS

In this paper, a two-dimensional numerical analysis method for clay is proposed, which reflects the real mesoscopic characteristics, and it can also be extended to other materials. The method is to convert the digital image containing meso features information into a numerical model for the calculation and analysis. With the powerful post-processing function of the finite-element software (ABAQUS), not only can the yield position in the observed area be obtained, but also the principal stress and meso shear stress of the whole field can be easily obtained.

The evolution laws of deflection angles and meso shear stresses at four points are different in the compression process. The change of deflection angle for each point is to adapt to the external loads, they all increase with the increasing of loads, but the change range near the pores is larger, and the plastic zone is prone to dislocations appearing. Moreover, the variation of the meso shear stress and the meso shear strength at each point is also affected by the internal pore characteristics. The weak structure formed by the pores is prone to the plastic zone, which leads to the evolution of secondary carriers. Obviously, the pore structures play a significant role in the evolution of the deflection angles and the meso shear stresses, especially around the larger and denser pores.

Clay samples depend on a stable backbone of the stress network with main and secondary carriers before failure. Once multiple secondary carriers form a through shear band, the clay samples will be destroyed.

The evolution of meso stress and the influence of pore characteristics in the shear band need further study.

REFERENCES

[1] Borja, R.I., Song, X.Y., Wu, W. 2013. Critical state plasticity. Part VII: Triggering a shear band in variably saturated porous media. Compu. Meth. Appl. Mech. Eng. 261–262, 66–82. DOI: 10.1016/j.cma.2013.03.008

[2] Lu, X. B., Yang, Z.S. 1999. Development of the shear band in saturated soil. Journal of Shanghai University 3, 199. DOI:10.1007/s11741-999-0058-8

[3] Gutierrez, M.S. 2007. Effects of constitutive parameters on shear band formation in granular soils. Soil Stress-Strain Behaviour: Measurement, Modelling and Analysis, Dordrecht, 146, 691-706. DOI: 10.1007/978-1-4020-6146-2_50

[4] Kumar, N., Luding, S., Magnanimo, V. 2014. Macroscopic model with anisotropy based on micro-macro information. Acta Mech., 225, 2319-2343. DOI: 10.1007/s00707-014-1155-8

[5] Shan, Y., Mo, H.H., Yu, S.M., Chen, J.S. 2016. Analysis of the maximum dynamic shear modulus and particle arrangement properties of saturated soft clay soils. Soil Mechanics and Foundation Engineering 53(4), 226-232. DOI: 10.1007/s11204-016-9390-8

[6] Bo, M.W., Arulrajah, A., Sukmak, P., Horpibulsuk, S., Leong, M. 2016. Mineralogy and geotechnical properties of ultrasoft soil from a nearshore mine tailings sedimentation pond. Marine Georesources and Geotechnology 34(8), 782-791. DOI: 10.1080/1064119X.2015.1094158

[7] Zhang, W., Liang, X.L., Tang, X.Y., Shi, B., Xu, Y.D., Xiao, R. 2017. Fine characterization of pore structure of Nanjing silty sand using micro-CT. Chinese Journal of Geotechnical Engineering 39(4), 683-689. DOI: 10.11779/CJGE201704013

[8] Wang, F.H., Xiang, W., Corely, T., Yeh J.T., Yuan, Y.F. 2018.The influences of freeze-thaw cycles on the shear strength of expansive soil treated with ionic soil stabilizer. Soil Mechanics and Foundation Engineering 55(3), 195-200. DOI: 10.1007/s11204-018-9525-1

[9] Xing, H.Z., Zhang, Q.B., Braithwaite, C.H., Pan, B., Zhao, J. 2017. High-speed photography and digital measurement techniques for geomaterials: fundamentals and applications. Rock Mech Rock Eng. 50, 1611-1659. DOI: 10.1007/s00603-016-1164-0

[10] Wang, P.P., Sang, Y., Shao, L.T., Guo, X.X. 2018. Measurement of the deformation of sand in a plane strain compression experiment using incremental digital image correlation. Acta Geotechnica 5,1-11. DOI : 10.1007/s11440-018-0676-z(0

[11] Yue, Z.Q., Chen, S., Tham, L.G. 2003. Finite element modelling of geomaterials using digital image processing. Computers and Geotechnics 30, 375-397. DOI: 10.1016/S0266-352X(03)00015-6

[12] Ghalehjough, B.K., Akbulut, S., Celik S. 2018. Effect of particle roundness and morphology on the shear failure mechanism of granular soil under strip footing. Acta Geotechnica Slovenica 1, 43-53. DOI: 10.18690/actageotechslov.15.1.43-53.2018

[13] Shao, L.T., Guo, X.X., Zhao, B.Y. 2018. Digital image measurement system for soil specimens in triaxial tests. Proceedings of China-Europe Conference on Geotechnical Engineering, pp 611-614. DOI: 10.1007/978-3-319-97112-4_136

[14] Amy, L.R., Sara, A., Olivier, C., Andrés, D.O. 2011. Characterization of mesoscale instabilities in localized granular shear using digital image correlation. Acta Geotechnica 6(4), 205-217. DOI: 10.1007/s11440-011-0147-2

[15] Jiang, M.J., Liu, J., Shen, Z.F. 2018. Investigating the shear band of methane hydrate-bearing sediments by FEM with an elasto-plastic constitute model. Bulletin of Engineering Geology and the Environment 77(3), 1015-1025. DOI:10.1007/s10064-017-1109-1

[16] Bayesteh, H., Ghasempour, T. 2018. Role of the location and size of soluble particles in the mechanical behaviour of collapsible granular soil: a DEM simulation. Computational Particle Mechanics 1-15. DOI: 10.1007/s40571-018-00216-x

[17] Nicot, F., Sibille, L., Hicher, P.Y. 2015. Micro-macro analysis of granular material behaviour along

proportional strain paths. Continuum Mechanics and Thermodynamics 27(1-2), 173-193. DOI: 10.1007/s00161-014-0347-8

[18] Li, B., Zhang, F.S., Gutierrez, M. 2015. A numerical examination of the hollow cylindrical torsional shear test using DEM. Acta Geotechnica 10, 449-467. DOI: 10.1007/s11440-014-0329-9

[19] Wang, W., He, P.L., Zhang, D.H. 2014. Finite element simulation based on soil mesostructures extracted from digital image. Soil Mechanics and Foundation Engineering 51(1), 17-22. DOI: 10.1007/s 11204-014-9248-x